ANNALS OF GEOPHYSICS, 69, 2026; doi:10.4401/ag-9513
OPEN ACCESS

Automatic downhole microseismic event location with an attention-enhanced fully convolutional neural network

Mingyuan Yang[1], Xiao Tian[*,1], Xiong Zhang[1], Zujian Yang[1], Yichong Chen[1]

(1) East China University of Technology, Engineering Research Center for Seismic Disaster Prevention and Engineering Geological Disaster Detection of Jiangxi Province, Nanchang, China

Article history: received December 7, 2025; accepted May 13, 2026

Abstract

Accurate and rapid localization of microseismic events in single-well downhole data is highly significant for microseismic monitoring. Although traditional methods, such as diffraction stacking and grid search, achieve high localization accuracy, they are computationally expensive, limiting their applicability for real-time microseismic monitoring. To address this limitation, we propose an attention-enhanced fully convolutional neural network (FCN-CBAM) for efficient single-well microseismic event localization. The method ingests three-component waveform data and outputs three one-dimensional Gaussian distributions representing the probability of the source location along the X, Y, and Z axes. The model is trained using 11,500 theoretical samples generated using the geometry and velocity model of the field data. Compared to traditional grid search methods, which require picking arrival time, calculating back-azimuth, and locating the 3D seismic source, the FCN-CBAM model can predict the event locations for field data within seconds, with prediction accuracy comparable to traditional methods. Furthermore, velocity perturbation and signal-to-noise ratio tests are performed to demonstrate the robustness and efficiency of our method.

Keywords: Deep Learning; Attention Mechanism; Artificial Intelligence; Event Localization; Downhole Microseismic Monitoring

1. Introduction

Microseismic monitoring for hydraulic fracturing has its roots in pioneering work at Sandia National Laboratories in the mid-1970s (Schuster, 1978) and was mainly applied to fracture imaging inversion methods in the 1980s. Since the 1990s, the study of fracturing-induced earthquakes has gradually attracted extensive attention from the international seismological community (Krishna et al., 2018; Atkinson et al., 2020). The challenges of monitoring, identifying, and managing earthquakes induced by underground industrial activities such as oil and gas extraction, geothermal development, and wastewater injection in Europe have been systematically summarized (Carannante et al., 2017; Grigoli et al., 2017).

Accurate localization of microseismic events is a fundamental step in microseismic monitoring, as it directly determines the reliability of fracture characterization and subsurface interpretation. Microseismic source localization methods are generally classified into two categories: travel-time-based and waveform-based approaches. The travel-time-based approach estimates source parameters by minimizing travel-time residuals, and can be implemented using various inversion strategies, among which the least-squares iterative method proposed by Bolt (1960) is one of the most widely used, forming the foundation for many absolute location techniques. Subsequent developments include improved algorithms such as HYPOINVERSE (Klein 2002), HYPOCENTER (Lienert and Havskov, 1995), and joint seismo-velocity inversion (Crosson, 1976). Relative localization methods, such as the master-event method (Spence, 1980) and the double-difference method (Waldhauser and Ellsworth, 2000), have also been proposed to improve accuracy by mitigating velocity-model errors. However, the travel-time-based location methods rely heavily on accurate P- and S-wave arrival times. Consequently, Waveform-based localization methods eliminate the need for manual phase picking. Examples include the Source Sweep Algorithm (SSA), which locates sources using a brightness function (Kao and Shan, 2004), and time-reversal imaging and full waveform inversion (FWI), which use the wave equation inversion (Virieux and Operto, 2009). Interferometric imaging estimates arrival time differences by waveform cross-correlation (Li et al., 2015), reducing dependence on first-arrival picking accuracy. These methods are well suited to low signal-to-noise ratios but remain computationally demanding and sensitive to velocity-model uncertainties.

In recent years, artificial intelligence technology has made breakthrough progress in the fields of computer vision, natural language processing, and speech recognition (Horvitz and Mitchell, 2024), and it has gradually expanded into the field of geophysics (Fernandes et al., 2025), showing broad prospects in seismology and seismic exploration (Mousavi and Beroza, 2022). In geophysical exploration, deep learning methods have been used for noise suppression (Yu et al., 2019), velocity model construction (Araya-Polo et al., 2018), data classification (Hajian et al., 2019; Casale and Pignatelli, 2024), fault identification (Guo et al., 2023), and reservoir prediction (Alfarraj and AlRegib, 2018; Wu et al., 2019), effectively improving the automation and intelligence of data processing. In seismology, the deep learning algorithms have been widely used in earthquake forecasting (Kiria et al., 2023), seismic phase identification (Zhu and Beroza, 2019), source localization, magnitude estimation (Mousavi and Beroza, 2020), and focal mechanism inversion (Tian et al., 2025). In particular, for source localization, traditional methods often rely on arrival-time picking or involve intensive computations, making them unsuitable for earthquake early warning or real-time hydraulic fracturing monitoring. Consequently, the application of deep learning to earthquake localization has yielded significant progress, as neural network models can be pre-trained for specific target areas to achieve efficient and accurate predictions.

Perol et al. (2018) first proposed ConvNetQuake, a convolutional neural network (CNN)-based model for earthquake detection and source localization that treated the localization task as a classification problem, marking the beginning of deep learning applications in earthquake location research. Subsequently, Kriegerowski et al. (2018) employed CNNs for direct source localization, while Zhang et al. (2020) formulated the localization problem as a regression task, using a fully convolutional network (FCN) to learn the mapping between multi-station waveforms and epicentral coordinates. Furthermore, van den Ende and Ampuero (2020) introduced a graph convolutional network (GCN)-based method for seismic source localization, enhancing model adaptability to irregular and complex array geometries.

Although deep learning has achieved remarkable progress in natural earthquake localization, its application in microseismic monitoring remains challenging due to the scarcity of high-quality labeled data, small focal scales, and low signal-to-noise ratios, which constrain model training and generalization. To address these challenges, in the area of surface microseismic localization, Vinard et al. (2021) employed a U-Net-based fully convolutional network to localize surface-recorded microseismic events, opening a promising direction for intelligent, data-driven processing. Building on this deep-learning paradigm, Zhang et al. (2022) introduced a localization strategy that couples neural networks with source-migration imaging, further enhancing both positioning accuracy and computational efficiency. Extending these advances to large-scale, real-scale scenarios, Gan et al. (2025) developed an automated deep learning framework specifically designed for surface monitoring, enabling robust and intelligent detection and localization of high volumes of microseismic events. In downhole microseismic localization, Huang et al. (2018) converted the recorded downhole microseismic waveforms into time-frequency representations and used the power and phase spectra of the cross-wavelet transform as inputs to a convolutional neural network, enabling automatic event characterization under noisy conditions. In a related line of work, Wamriew et al. (2022) employed distributed acoustic

sensing (DAS) data from downhole monitoring and integrated deep learning to realize intelligent microseismic detection and analysis in realistic field environments.

Currently, many deep learning-based microseismic localization methods have been developed for surface monitoring systems and various downhole configurations. However, their application to single-well downhole monitoring with dense borehole receiver arrays remains relatively limited. To further promote the application of artificial intelligence in single-well downhole microseismic event localization, a fully convolutional neural network incorporating a convolutional block attention module (FCN-CBAM) is proposed and developed for downhole localization. For a specific downhole monitoring system, forward modeling is first performed to generate the training dataset. The trained neural network is then applied to field data for event localization, and the predicted location results are compared with those obtained using traditional methods.

2. Training data generation

2.1 Theoretical data

The field data used in this study are acquired from a typical downhole microseismic monitoring configuration during hydraulic fracturing. As shown in Fig. 1, twelve three-component (3C) receivers are deployed in a vertical monitoring well at depth ranging from 2800 m to 3020 m, with an interval of 20 m. The potential source coordinates range from 280 to 430 m in the X direction, −200 to 300 m in the Y direction, and 3,050 to 3,200 m in the Z direction, with a grid spacing of 3 m. A Ricker wavelet is adopted as the source wavelet. The blue and red lines in Fig. 1a represent the P-wave and S-wave velocity models used in this research, both extracted from well-logging data.

In this study, the theoretical training dataset is constructed based on the geometry and velocity model of the field data to train the neural network model. The trained model is then directly applied to the field data.

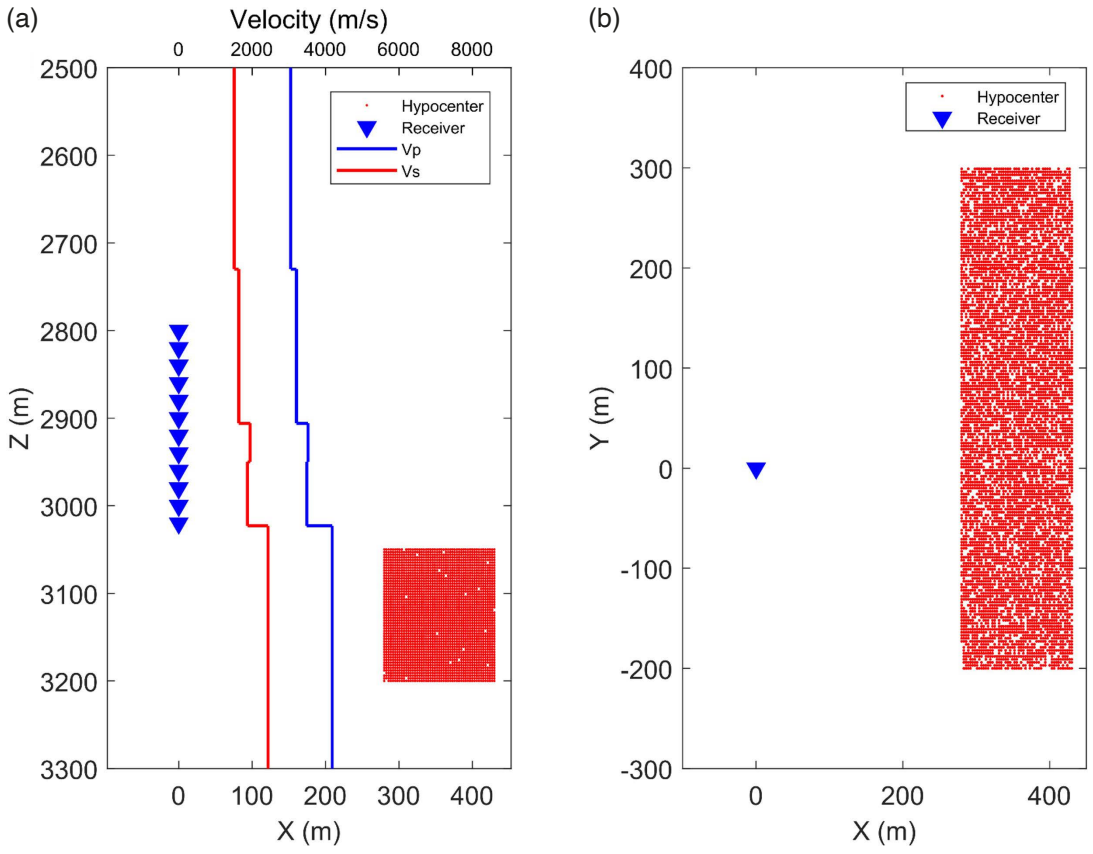

Figure 1. Different views of the acquisition geometry. (a) Depth view of the experiment geometry, where blue triangles and red dots represent receiver and source locations, respectively. The blue and red lines denote the P-wave and S-wave velocity models. (b) Map view of the experiment geometry.

The generalized inverse transmission coefficient method is employed to simulate theoretical microseismic waveforms. First, the study area is discretized into grids, Green's functions are calculated for each potential grid point, and a Green's function library is generated. Subsequently, convolution is performed between the source time function and Green's function, and the theoretical waveform is synthesized by integrating multiple parameters, thereby obtaining synthetic seismic records that incorporate both source information and medium response. Each synthetic waveform has a duration of 512 ms (corresponding to 512 sampling points) with a sampling rate of 1,000 Hz.

2.2 Data Enhancement Techniques

In this section, data augmentation strategies are employed to minimize discrepancies between theoretical and field waveforms. First, background noise extracted from field data is added to the theoretical waveforms to simulate field data recording conditions. The noise amplitudes are adjusted to produce signal-to-noise ratios (SNRs) in the range of 8-20, within which the P-waves remain clearly distinguishable and are not obscured by noise. This SNR range is determined based on statistical analysis of the field records, ensuring that the simulated noise levels are consistent with realistic monitoring conditions. Additionally, random time-axis shifts are applied to emulate variations in event origin times, thereby eliminating the need for known source origin times. Finally, all waveform channels are normalized to the range [−1,1] to improve training stability and model generalization. Figure 2 illustrates the data preprocessing and augmentation process. Figure 2a shows the original waveforms, while Fig. 2b displays the waveforms after normalization, noise addition, and random time shifting.

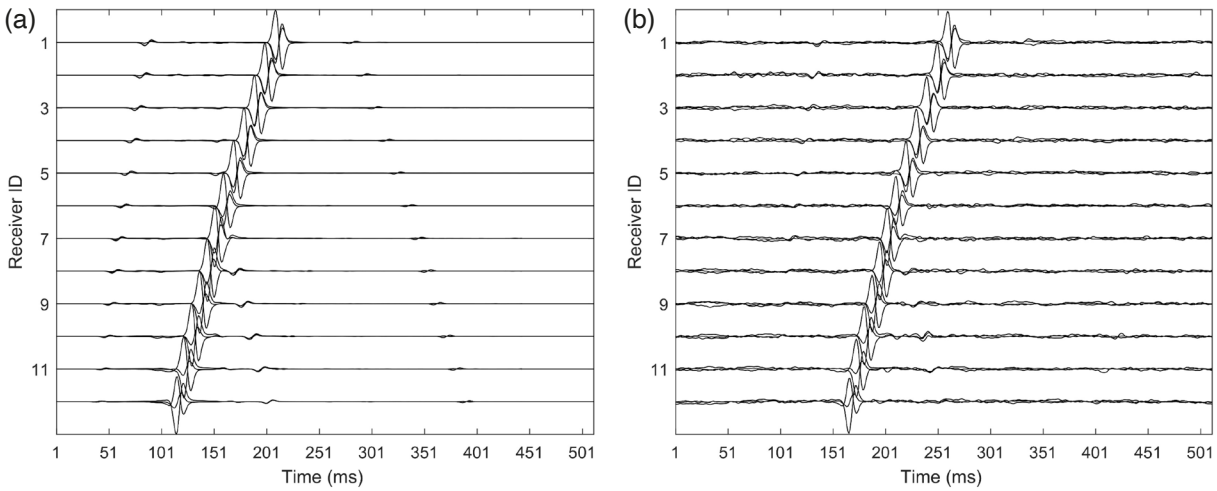

Figure 2. Data augmentation for microseismic waveforms. (a) Original three-component (3C) waveforms recorded by twelve receivers within a 512-ms window. (b) Waveforms after normalization, noise addition, and random time shifting.

3. Method

In this section, a fully convolutional network (FCN) designed for the automatic localization of single-well microseismic events is presented. FCNs are end-to-end deep learning models that employ stacked convolutional layers to automatically extract features from input images. They are particularly well suited for pixel-level semantic segmentation and eliminate many cumbersome steps in traditional pipelines, thereby improving both efficiency and accuracy.

Figure 3 shows the architecture of the proposed neural network for microseismic localization. The input consists of multi-component waveforms recorded by twelve downhole receivers within a 512 ms window. The network utilizes three one-dimensional (1D) Gaussian distributions to represent the source location along the X, Y, and Z dimensions. Each Gaussian distribution is centered on the true source coordinate along its corresponding axis. Through multiple convolutional layers, the network learns the characteristic features of the waveform data and

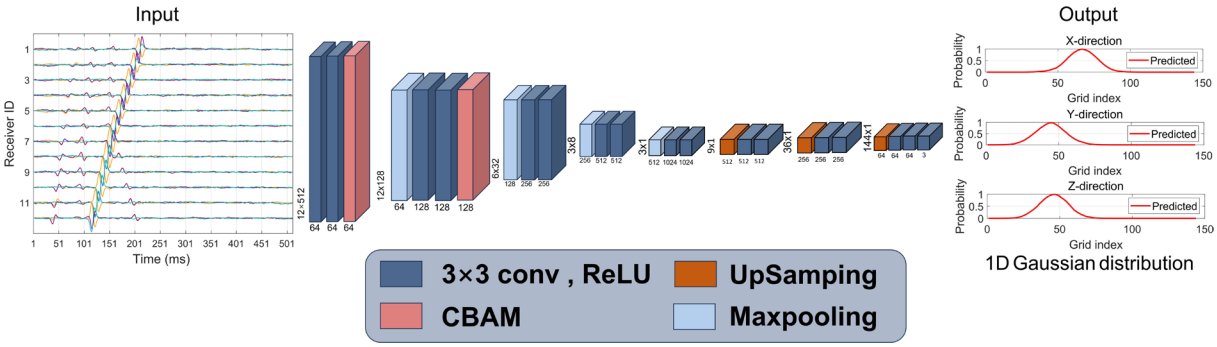

Figure 3. FCN-CBAM architecture for microseismic event localization. Input: waveforms data (12 × 512 × 3). The network adopts an encoder-decoder structure composed of 3 × 3 convolutional layers with ReLU (Rectified Linear Unit) activation, max-pooling, and upsampling operations. The ReLU activation introduces nonlinearity by setting all negative values to zero while keeping positive values unchanged, which allows the network to efficiently learn complex features. CBAM modules are embedded after the initial convolutional stages to enhance feature extraction. Output: three 1-D Gaussian distributions representing the hypocenter probability along the X, Y, and Z axes.

outputs a 1-D Gaussian probability-density map. The peak of this map corresponds to the most probable hypocenter location, while the peak amplitude reflects the confidence level of the prediction.

The input sample has a length of 512, but the information most relevant for localization is primarily concentrated within the P-wave and S-wave phases. To enhance the model's accuracy, an attention mechanism is incorporated into the FCN architecture. The Convolutional Block Attention Module (CBAM), first introduced by Woo et al. (2018), is a lightweight attention mechanism designed to enhance the feature representations of convolutional neural networks (CNNs). CBAM consists of two components: a Channel Attention Module (CAM) and a Spatial Attention Module (SAM). These modules compute adaptive attention maps along the channel and spatial dimensions of the input feature maps, respectively, thereby directing the network's focus to salient features and improving both representational capacity and generalization performance (Zhou et al., 2023). As shown in Fig. 4, we begin with the original feature map (Input Feature). The input feature map is then processed by a Channel Attention Module (CAM) and a Spatial Attention Module (SAM), yielding the final refined feature map (Refined Feature). In this study, CBAM modules are inserted after the first and second convolutional blocks. The FCN-CBAM architecture is shown in Fig. 3.

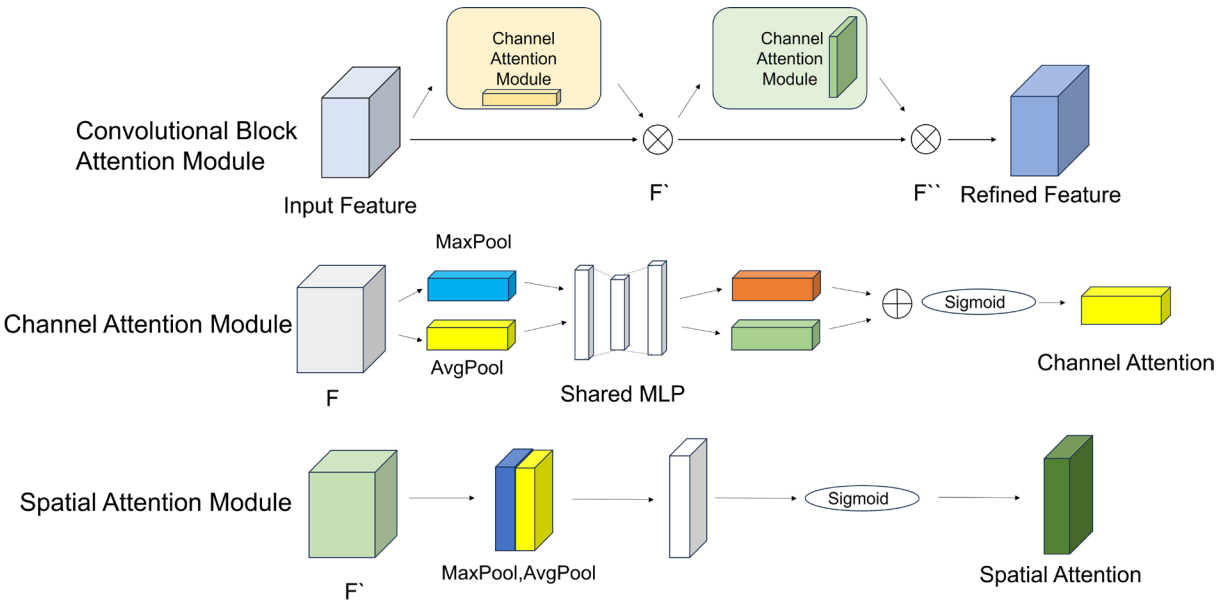

Figure 4. Convolutional Block Attention Module (CBAM) architecture.

4. Numerical experiments

4.1 Theoretical data training and validation

A total of 12,500 synthetic samples are generated, with 11,500 used for training and validation (split in a 9:1 ratio) and 1,000 reserved for testing. Figure 5 illustrates the convergence of the FCN and FCN-CBAM models after 100 training epochs.

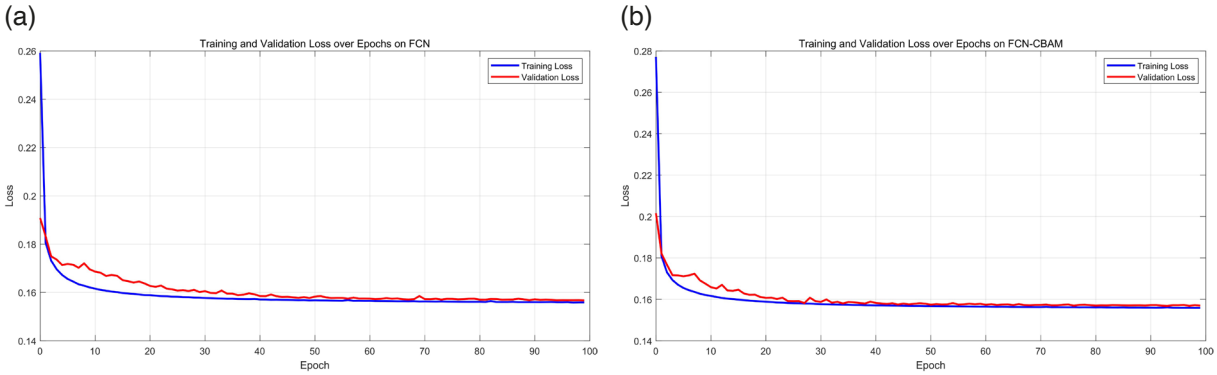

Figure 5. Loss curves of training and validation set. (a) FCN; (b) FCN-CBAM.

The trained FCN-CBAM model is applied to predictions on test dataset, as shown in Fig. 6. Figure 6a displays the synthetic waveform, while Fig. 6b includes three subplots illustrating the probability distributions of the predicted and true values along the X, Y, and Z axes (red: prediction; blue: ground truth). The predicted and true curves exhibit strong consistency across all three directions, particularly at the peak locations, demonstrating accurate and reliable hypocenter localization.

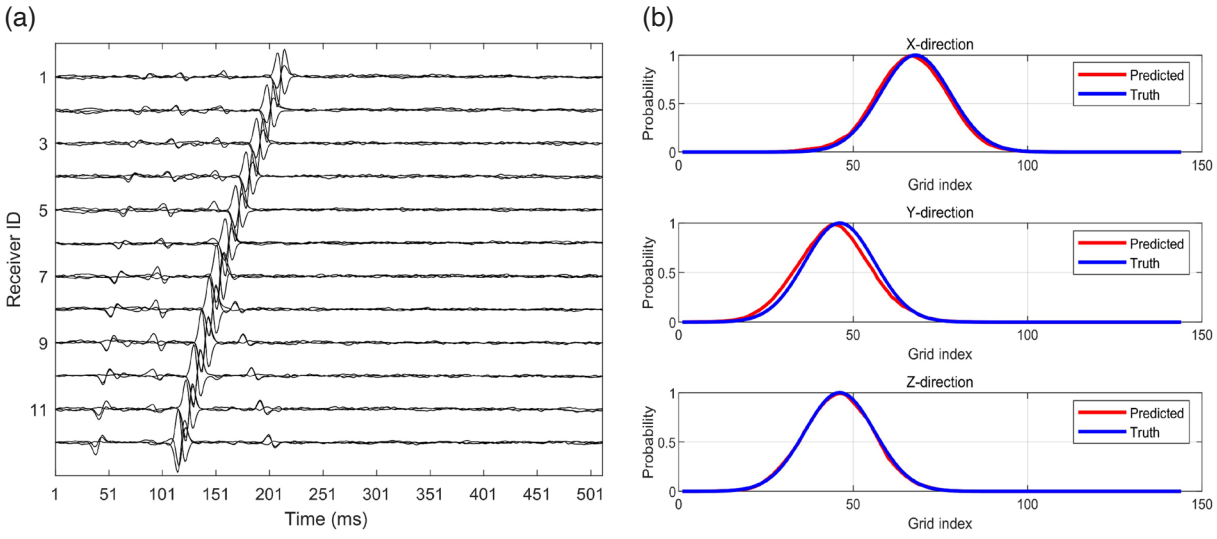

Figure 6. Waveforms and prediction results for the FCN-CBAM model. (a) One waveform from the test dataset. (b) One-dimensional Gaussian distributions along the X, Y, and Z axes showing predicted (red) and true (blue) values.

To further evaluate the performance of the trained FCN-CBAM model, the entire test dataset is input into the network, and scatter plots of predicted versus ground-truth values are generated in Fig. 7 to assess the correlation between predictions and actual locations. The scatter plots for all three axes demonstrate a strong positive correlation between predicted and true values, indicating that the trained FCN-CBAM model can accurately invert the locations

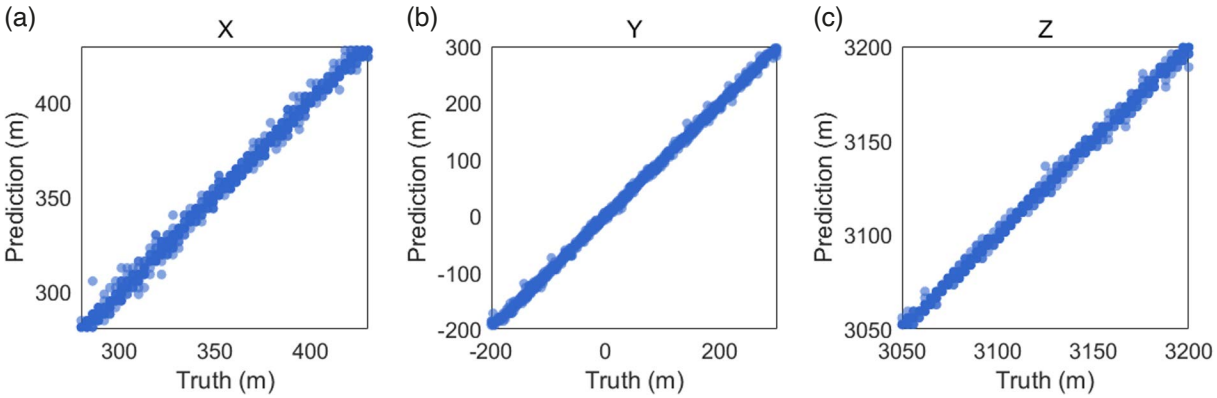

Figure 7. Scatter plots of predictions versus ground truth values of event locations of the FCN-CBAM model.

of single-well monitored microseismic events. As shown in Fig. 7, the FCN-CBAM model achieves strong predictive performance. The results indicate that FCN-CBAM is theoretically feasible for localization tasks. By combining a fully convolutional network (FCN) with the Convolutional Block Attention Module (CBAM), the model effectively enhances feature extraction and attention to salient regions. Using one-dimensional labels for supervision enables more precise capture of spatial and positional characteristics, yielding high localization accuracy. Both theoretical analysis and experimental results demonstrate stable prediction and localization under varying conditions, providing useful reference value for related applications.

Finally, the performance of the FCN and FCN-CBAM models is evaluated using the test dataset. The predicted locations are compared with the true hypocenters, and the resulting localization errors are visualized as histograms (Fig. 8). Analysis of the test dataset indicates that FCN-CBAM performs slightly better than FCN. For the 1,000 events, the mean localization errors along the X, Y, and Z axes are detailed in the Fig. 8, with mean values of 2.47 m, 3.58 m, and 1.82 m, respectively.

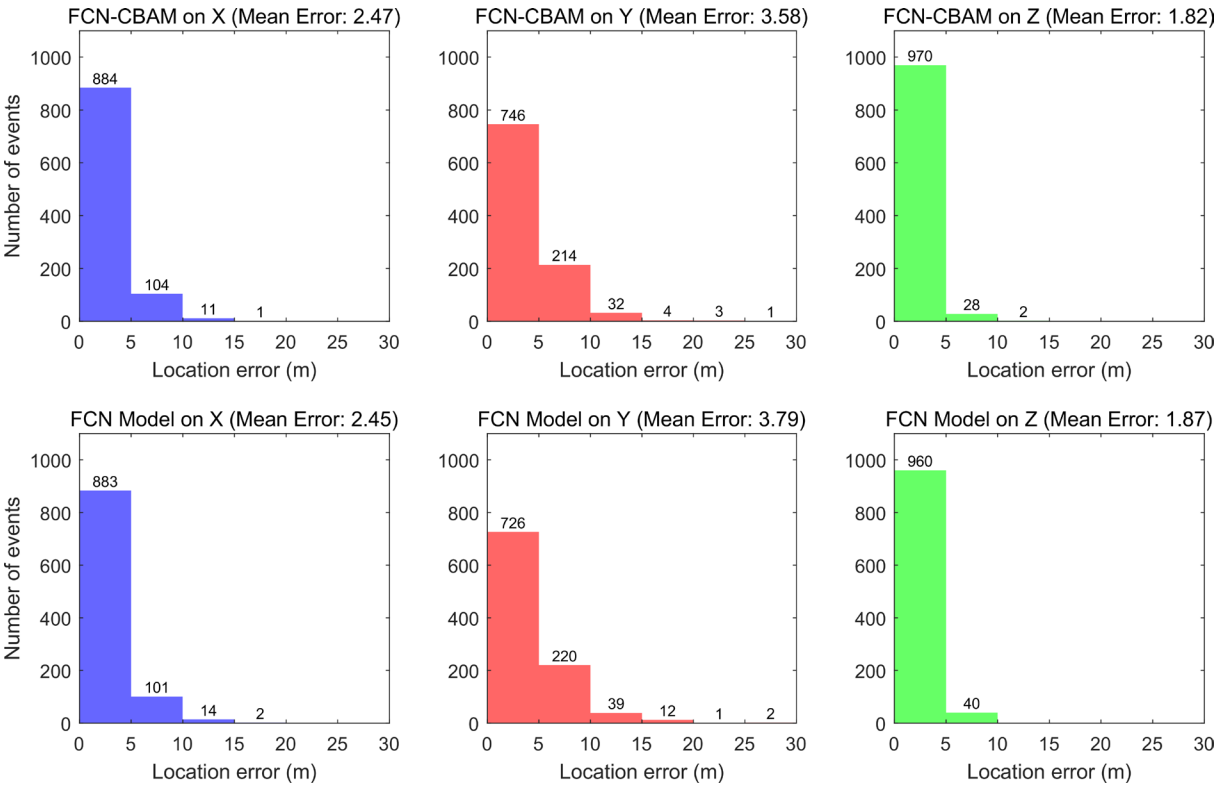

Figure 8. Histograms of the location errors for the test dataset, comparing the performance of the FCN and FCN-CBAM models.

4.2 Field Data Application

To evaluate the practical applicability and generalization capability of the FCN-CBAM model trained on synthetic data, it is further tested using field microseismic recordings. The dataset used in this study is provided by BGP, China National Petroleum Corporation (CNPC). Since ground-truth locations are unavailable for field data, the model's predictions are compared with results obtained using a conventional grid-search localization method. The workflows of both localization approaches are summarized in Fig. 9. For the conventional grid-search localization method, the arrival times of both P- and S-waves must first be manually picked. Because the velocity model used for the field data is one-dimensional (1D layered), the grid-search method can only determine two-dimensional (2D) source locations. All events are initially located within a 2D profile and subsequently projected into 3D space using event azimuths derived from a separate analysis of the initial P-wave polarizations. In contrast, once the FCN-CBAM model is trained, only the waveform data need to be input into the network, and the model can predict 3D source locations within seconds.

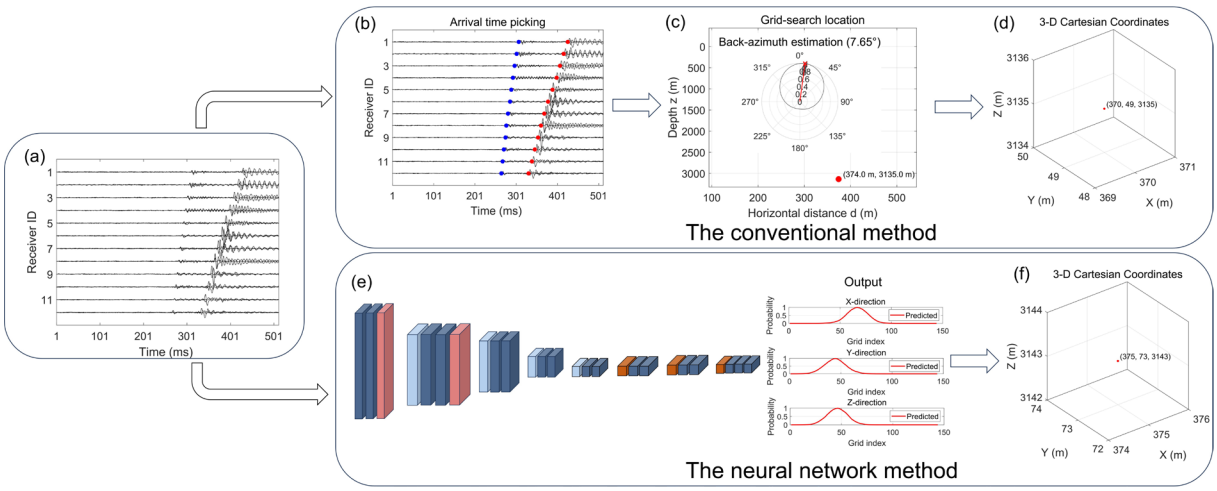

Figure 9. Integrated workflow for microseismic event localization using grid search and a neural network model. (a) Three component waveforms recorded by the downhole multi-receiver array. (b) Picked P-wave (blue) and S-wave (red) arrival times. (c) Candidate source location obtained from the grid-search method (horizontal distance vs. depth). Back-azimuth estimation. (d) Source location from the conventional method shown in 3-D Cartesian coordinates. (e) FCN-CBAM. (f) Source location predicted by the neural network model in 3-D Cartesian coordinates.

A field test dataset containing 1,506 events was constructed and used for localization. The predicted locations obtained from the FCN-CBAM model are compared with those derived from the conventional grid-search method to evaluate its reliability and robustness. As shown in Fig. 10, the scatter plot presents the localization results for microseismic events induced during hydraulic fracturing. The blue dots represent the locations predicted by the FCN-CBAM model, while the red dots indicate locations obtained with the conventional grid-search location method. Results show that both methods yield comparable locations. The clustering of events around the production well (shown by the green line in Fig. 10) further supports the validity of the predicted locations. To quantitatively assess the differences between the FCN-CBAM model and the grid-search method, we performed a statistical analysis of the location discrepancies, which are presented as histograms in Fig. 11.

Relative to grid search method, the FCN-CBAM model yields mean localization errors of 23.2 m, 46.9 m, and 23.4 m along the X-, Y-, and Z-axes, respectively. These findings indicate that the FCN architecture with CBAM represents a promising approach for microseismic event localization and can support microseismic monitoring and safety assessment in hydraulic-fracturing operations.

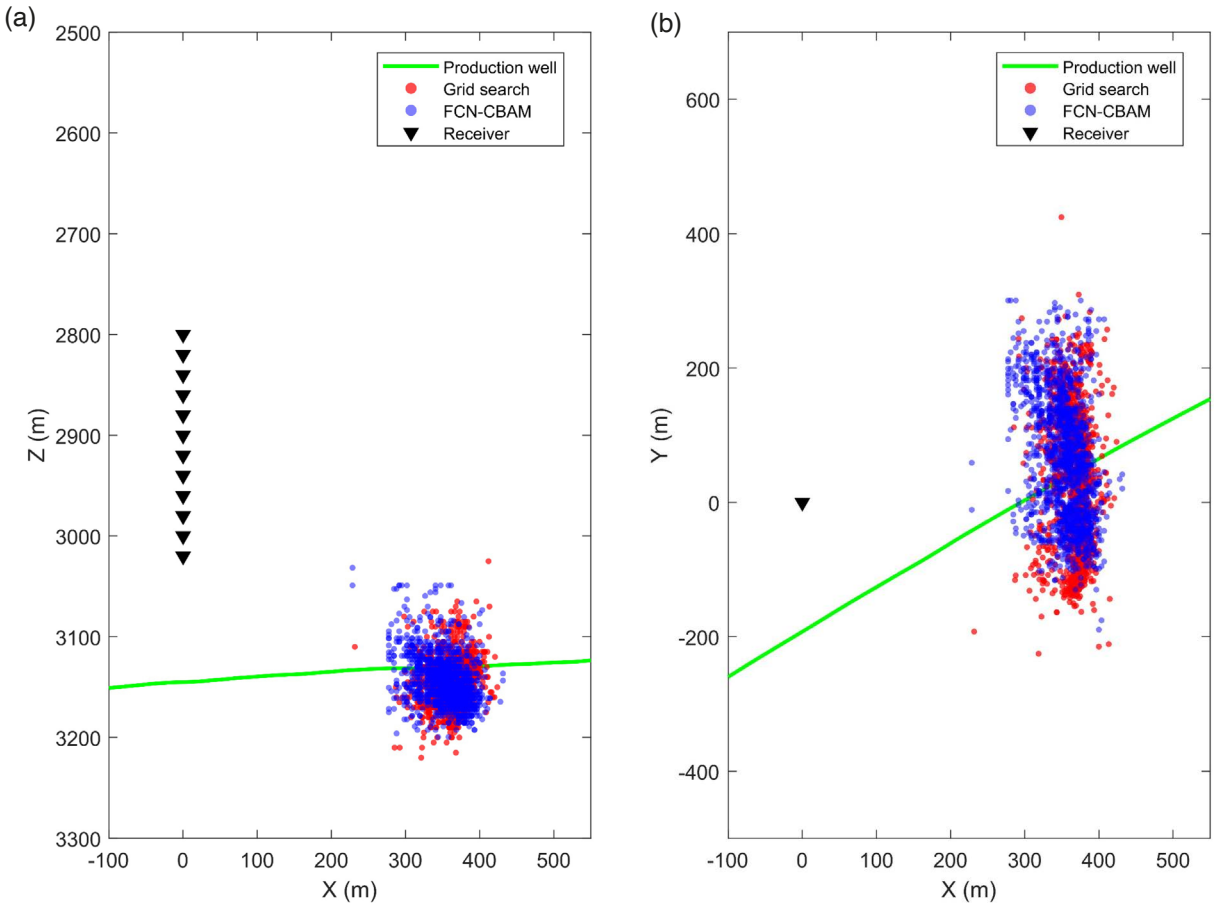

Figure 10. Field microseismic locations: grid search vs FCN-CBAM. (a) Cross-section(X-Z). (b) Plan view (X-Y). The green line shows the production well trace in map view. Red dots: grid-search locations; blue dots: FCN-CBAM locations; Black inverted triangles indicate the receivers.

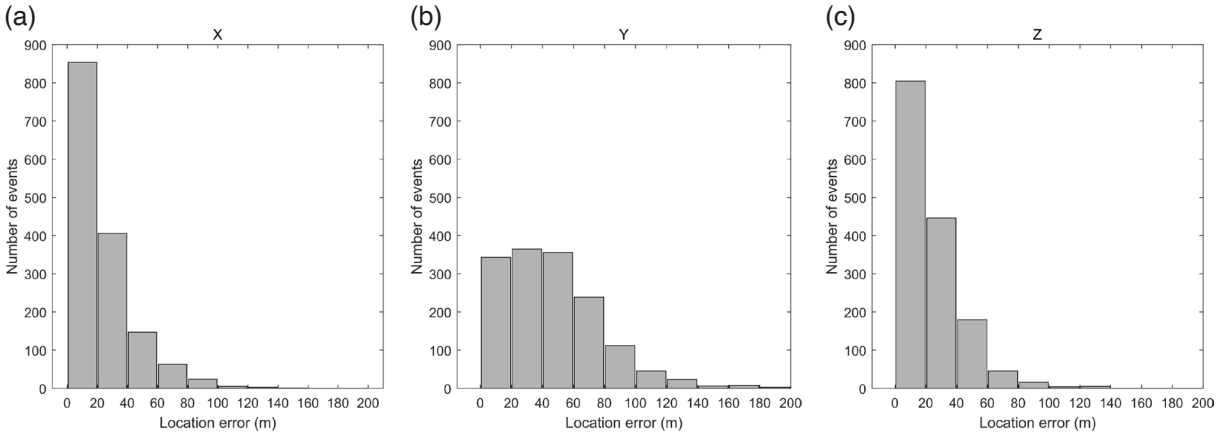

Figure 11. Localization-error distributions on field data (comparison with the grid-search baseline). (a) X (b) Y (c) Z.

5. Discussion

5.1 Velocity model perturbation experiment

To evaluate the robustness of the FCN-CBAM model in predicting source locations under inaccurate velocity models, random perturbations are applied to the original layered velocity model. Figures 12a, 12b, and 12c show

perturbations of 10%, 20%, and 30%, respectively, where dashed lines represent the perturbed velocities and solid lines indicate the true velocities. A total of 1,000 synthetic events are randomly selected for prediction. We then analyze the localization errors across perturbation levels to quantify the impact of velocity-model variations on hypocenter accuracy. The mean localization errors under each perturbation level are summarized in Table 1.

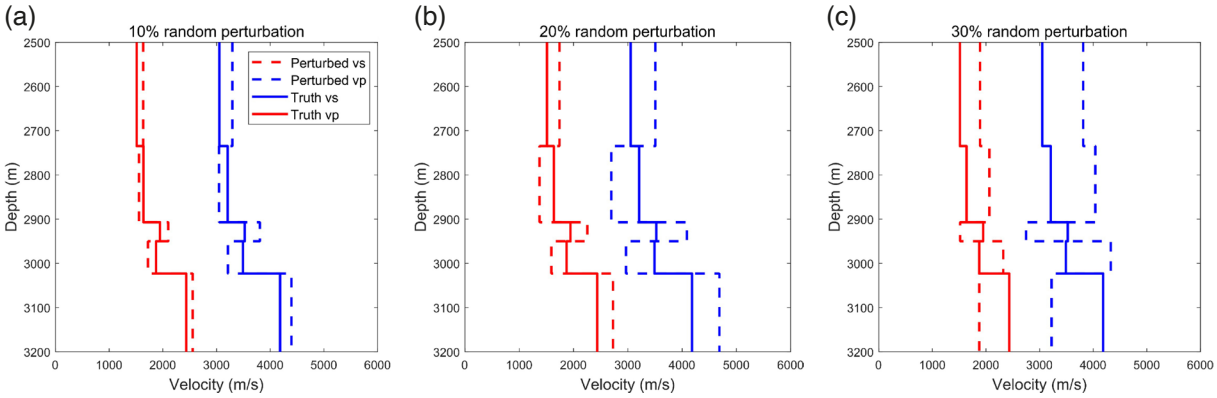

Figure 12. Layered velocity models with random perturbations (blue: P-wave velocity; red: S-wave velocity). Solid lines: true model; dashed lines: perturbed. (a) 10% perturbation; (b) 20% perturbation; (c) 30% perturbation.

Table 1. Mean localization error under different velocity-model perturbations.

Random perturbation	X direction (m)	Y direction (m)	Z direction (m)
10%	20.7	11.1	12.6
20%	45.0	22.2	29.6
30%	59.6	44.8	61.8

Table 1 shows that as the velocity perturbation increases from 10% to 30%, the mean localization errors along the X, Y, and Z directions rise markedly – for example, the mean error along X increases from 20.7 m to 59.6 m, along Y from 11.1 m to 44.8 m, and along Z from 12.6 m to 61.8 m. These results indicate a pronounced adverse effect of velocity perturbations on localization accuracy, with errors escalating sharply at higher perturbation levels. They underscore the critical importance of an accurate subsurface velocity model – particularly the fidelity of P- and S-wave velocities – for precise microseismic hypocenter localization. The observed error growth implies that, under strong perturbations, uncertainty in the velocity field directly and severely degrades localization accuracy; therefore, improving the velocity model and mitigating perturbation effects are essential for enhancing localization performance.

5.2 Model Applicability and Transfer Learning Enhancement

Although the proposed framework is initially developed based on a specific velocity model and borehole configuration, it cannot be directly applied to other geological settings. To address this limitation, a transfer learning strategy is introduced to improve the adaptability and generalization capability of the model. Specifically, as shown in Fig. 13b, a perturbed velocity model is constructed by introducing 10% random variations to the original P-wave and S-wave velocity profiles, thereby simulating realistic velocity uncertainties. In addition, a modified observation system is designed, where a vertical receiver array is deployed within a depth range of 2800-3160 m with a spacing of 30 m. Events are randomly distributed within a confined region (X: 300-400 m, Y: −100-100 m, Z: 3050-3200 m), representing a typical reservoir-scale monitoring scenario (Fig. 13a).

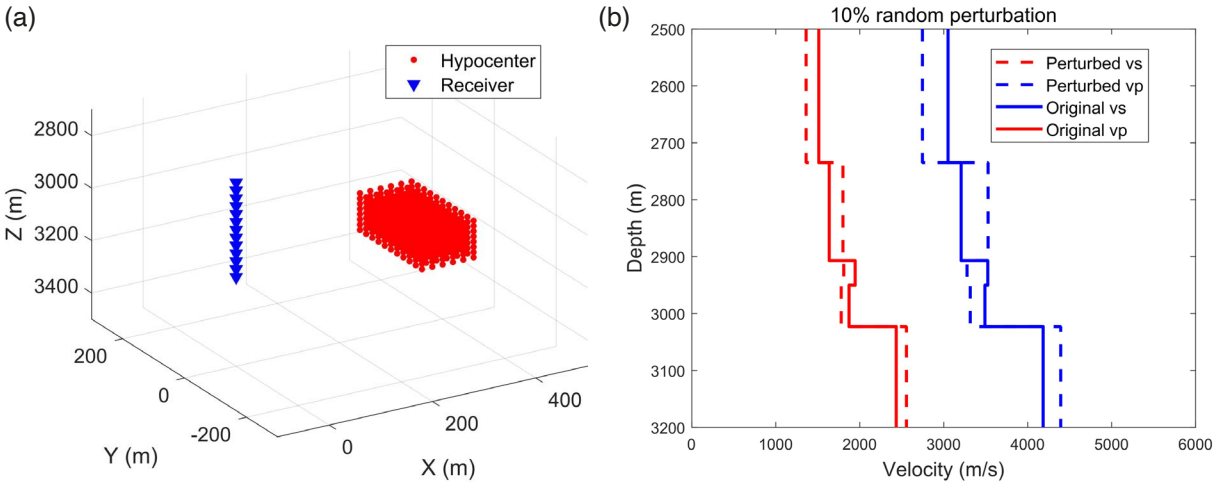

Figure 13. Observation system configuration. (a) Distribution of hypocenters (red dots) and receivers (blue triangles). (b) Layered velocity models with random perturbations (blue: P-wave velocity; red: S-wave velocity). Solid lines denote the original model, and dashed lines denote the perturbed model.

Based on the modified velocity model and acquisition geometry, multiple datasets with varying sample sizes are generated to evaluate model performance under domain shifts. Two training strategies are considered: (1) direct training using the newly generated datasets, and (2) transfer learning, in which the pretrained model is fine-tuned using a limited amount of new data.

As shown in Fig. 14, the localization performance of transfer learning and direct training is compared at sample sizes of 200, 1000, and 5000. The transfer learning approach outperforms direct training across all sample sizes, with the most prominent advantage observed in the small-data regime (200 samples): it reduces the average localization errors in X/Y/Z directions from ~26.8/21.9/14 m to ~7.3/7/6 m, representing a 57%-69% error reduction. As the

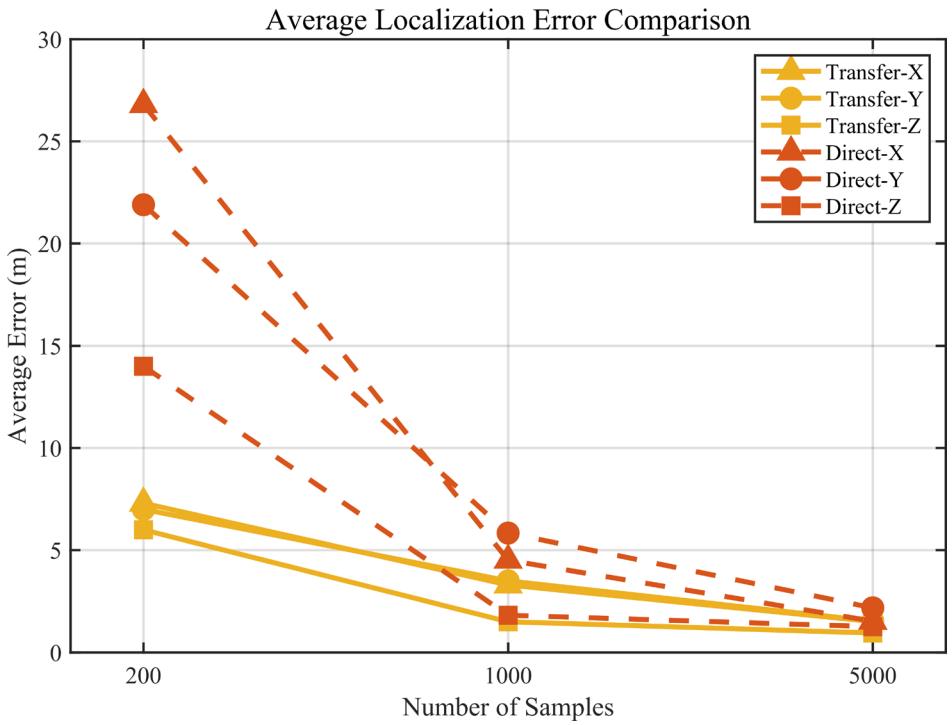

Figure 14. Comparison of average localization errors. The average errors in X, Y, and Z directions are shown for transfer learning (yellow solid lines: Transfer-X/Y/Z) and direct training (red dashed lines: Direct-X/Y/Z) under different training sample sizes (200, 1000, and 5000).

number of training samples increases to 1000 and 5000, the localization errors of both methods decrease gradually, while transfer learning consistently converges to a lower error level (~1-2 m across all directions at 5000 samples), effectively mitigating the impact of subsurface velocity uncertainties on localization accuracy.

These findings suggest that, although the proposed model is initially trained on a specific velocity model and observation system, the integration of transfer learning enables effective knowledge transfer across different domains. This reduces the dependence on large-scale retraining and improves the feasibility of applying the model to diverse geological settings. Future work may further explore domain adaptation techniques and multi-model training strategies to achieve broader generalization across complex subsurface environments.

5.3 Relationship between SNR and localization error

To assess the robustness and accuracy of the FCN-CBAM model under varying noise levels, a detailed analysis of prediction errors is conducted across different signal-to-noise ratios (SNRs). Figure 15a presents Z-component waveforms under different SNR levels. Considering that field noise is predominantly concentrated in the low-frequency range, a 4th-order Butterworth band-pass filter (20-200 Hz) was applied as a preprocessing step to suppress noise components while preserving useful seismic signals. To quantitatively assess the effectiveness of noise suppression, we compared the proportional distribution of localization errors before and after filtering under different SNR levels (0-2, 2-4, 4-6, 6-8, and 8-10 dB), as shown in Fig. 15b. The horizontal axis denotes SNR (dB) and the vertical axis denotes the proportion of samples within specified error ranges.

At low SNR levels (0-2 dB and 2-4 dB), localization errors are dominated by large deviations (≥20 m). Specifically, nearly 100% of events exceed this threshold at 0-2 dB, and approximately 96% at 2-4 dB. As the SNR increases, localization performance improves significantly. When SNR reaches ≥6 dB, the proportion of events with errors below 20 m increases markedly, reaching approximately 77% at 8-10 dB. This trend is consistent with the waveform characteristics shown in Fig. 15a, where P-wave arrivals are barely distinguishable at low SNRs but become increasingly clear as SNR increases.

Furthermore, the application of band-pass filtering effectively reduces large localization errors, particularly under low-to-moderate SNR conditions (2-6 dB). At moderate SNR levels (e.g., 6-8 dB), filtering significantly increases the proportion of accurate predictions (<20 m), indicating enhanced robustness. At high SNR conditions (8-10 dB), both filtered and unfiltered data yield stable performance, although filtering still provides a slight improvement in error distribution. These results demonstrate that the proposed filtering-based noise mitigation strategy effectively suppresses noise-induced errors and improves model robustness, especially under low-to-moderate SNR conditions.

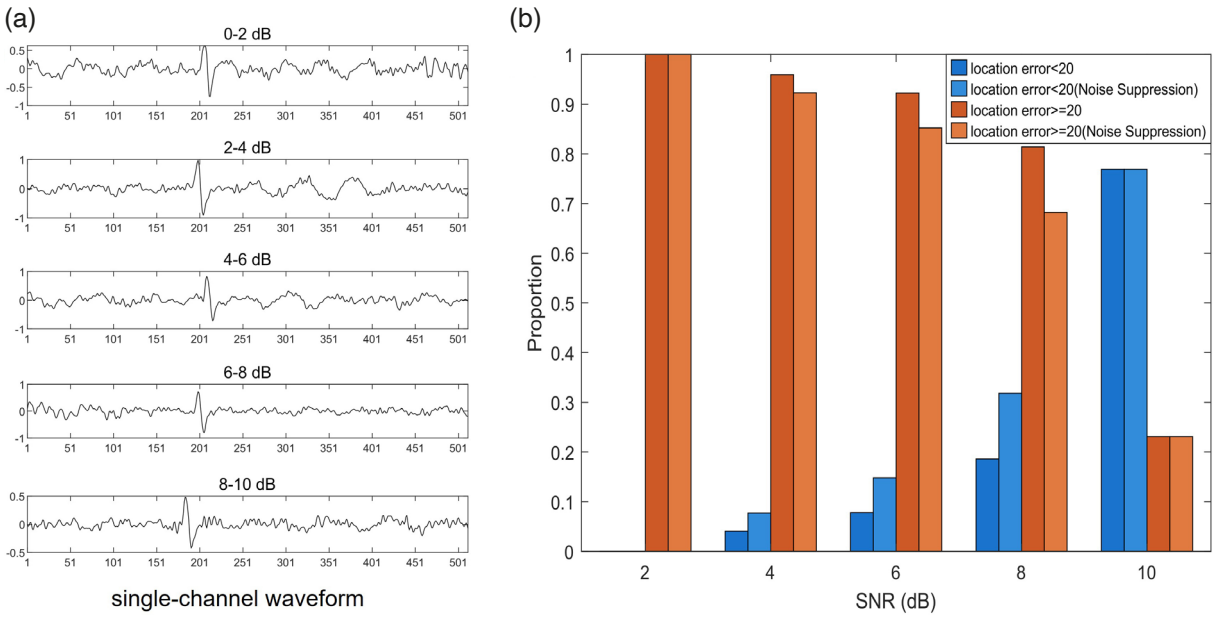

Figure 15. (a) Z-component waveforms at different SNRs. (b) Proportional distribution of localization errors under different signal-to-noise ratios before and after noise suppression.

6. Conclusion

This study presents a single-well microseismic localization approach based on a fully convolutional network augmented with a channel-spatial attention mechanism (FCN-CBAM). Upon inputting downhole three-component waveforms into the neural network, the model generates three one-dimensional Gaussian probability distributions corresponding to the X, Y, and Z coordinates, enabling rapid and accurate source localization. By incorporating data augmentation techniques, such as band-pass filtering, normalization, noise injection, and time shifting, this method demonstrates robust stability and generalization across varying noise levels and velocity model perturbations. It also significantly reduces computational costs compared to the grid search method, thereby meeting real-time monitoring requirements.

This study proposes a deep learning-based framework offering a practical solution for unconventional oil and gas development. Currently, the trained models are designed for specific work areas, and achieving generalization across arbitrary velocity models and geometries remains a challenge.

Data availability statement. The codebase for FCN-CBAM, together with a reproducible numerical example, is available on GitHub (https://github.com/XiaoTian09/FCN-CBAM). The repository contains the network architecture and a representative test case. Owing to the size of the full training datasets, they are not released; however, a 2,000-sample demo dataset is provided to enable users to execute the network and replicate the training pipeline.

Acknowledgements. This study was supported by National Natural Science Foundation of China Grant (No. 42004040, U2239204), Natural Science Foundation of Jiangxi Province Grant (20242BAB25190).

References

Alfarraj, M. and G. AlRegib (2018). Petrophysical property estimation from seismic data using recurrent neural networks, SEG Technical Program Expanded Abstracts 2018, Society of Exploration Geophysicists, Houston, 2141-2146, doi:0.48550/arXiv.1901.08623.

Araya-Polo, M., J. Jennings, A. Adler and T. J. Dahlke (2018). Deep-learning tomography, Lead. Edge, 37, 1, 58-66, doi:10.1190/tle37010058.1.

Atkinson, G. M., D. W. Eaton and N. Igonin (2020). Developments in understanding seismicity triggered by hydraulic fracturing, Nat. Rev. Earth Environ., 1, 5, 264-277, doi:10.1038/s43017-020-0049-7.

Bolt, B. A. (1960). The Revision of Earthquake Epicentres, Focal Depths and Origin-Times using a High-Speed Computer, Geophys. J. Int., 3, 4, 433-440, doi:10.1111/j.1365-246X.1960.tb01716.x.

Carannante, S., E. D'Alema, S. Lovati, M. Massa et al. (2017). Feasibility study for the microseismic monitoring of the natural gas reservoir of "Sant'Alberto"(Po Plain, Italy), Ann. Geophys., 60, 2, S0217, doi:10.4401/ag-7111.

Casale, P. and A. Pignatelli (2024). Use of deep learning to improve seismic data quality analysis, Ann. Geophys., 67, 3, SE320, doi:10.4401/ag-9055.

Crosson, R. S. (1976). Crustal structure modeling of earthquake data: 1. Simultaneous least squares estimation of hypocenter and velocity parameters, J. Geophys. Res., 81, 17, 3036-3046, doi:10.1029/JB081i017p03036.

Fernandes, G. L., F. Figueiredo, R. S. Hatushika, M. L. Leão et al. (2025). A systematic review of deep learning for structural geological interpretation, Data Min. Knowl. Disc., 39, 1, 3, doi:10.1007/s10618-024-01079-y.

Gan, Z., X. Tian, X. Zhang and M. Dai (2025). Automatic location of surface-monitored microseismicity with deep learning, Earthquake Res. Adv., 5, 100355, doi:10.1016/j.eqrea.2024.100355.

Grigoli, F., S. Cesca, E. Priolo, A. P. Rinaldi et al. (2017). Current challenges in monitoring, discrimination, and management of induced seismicity related to underground industrial activities: A European perspective, Rev. Geophys., 55, 2, 310-340, doi:10.1002/2016RG000542.

Guo, L., R. Xiong, J. Zhao, H. Wang et al. (2023). Seismic Fault Identification Based on Multi-Scale Dense Convolution and Improved Long Short-Term Memory Network, IEEE Access, 11, 124114-124128, doi:10.1109/ACCESS.2023.3 328630.

Hajian, A., F. Cannavò, F. Greco and G. J. Nunnari (2019). Classification of Mount Etna (Italy) volcanic activity by machine learning approaches, Ann. Geophys., 62, 2, VO231, doi:10.4401/ag-8049.

Horvitz, E. and T. M. Mitchell (2024). Scientific progress in artificial intelligence: History, status, and futures, in Realizing the Promise and Minimizing the Perils of Artificial Intelligence for the Scientific Community K. H. Jamieson, A. M. Mazza and W. Kearney (Editors), University of Pennsylvania Press, Philadelphia, ISSN:9781512827484.

Huang, L., J. Li, H. Hao and X. Li (2018). Micro-seismic event detection and location in underground mines by using Convolutional Neural Networks (CNN) and deep learning, Tunn. Undergr. Space Technol., 81, 265-276, doi:10.1016/j.tust.2018.07.006.

Kao, H. and S. J. Shan (2004). The Source-Scanning Algorithm: mapping the distribution of seismic sources in time and space, Geophys. J. Int.,157, 2, 589-594, doi:10.1111/j.1365-246X.2004.02276.x.

Kiria, T., T. Chelidze, G. Melikadze, T. Jimsheladze et al. (2023). Earthquake forecast by imbalance machine learning using geophysical predictors, Ann. Geophys., 66, 6, SE636, doi:10.4401/ag-8946.

Klein, F. W. (2002). User's Guide to HYPOINVERSE-2000, a FORTRAN program to solve for earthquake locations and magnitudes, Open File Report, 171, U. S. Geological Survey, Reston, 123, doi:10.3133/ofr02171.

Kriegerowski, M., G. M. Petersen, H. Vasyura-Bathke and M. Ohrnberger (2018). A Deep Convolutional Neural Network for Localization of Clustered Earthquakes Based on Multistation Full Waveforms, Seismol. Res. Lett., 90, 2A, 510-516, doi:10.1785/0220180320.

Krishna, S., H. Sreenivasan and R. R. Nair (2018). Hydraulic fracture studies of reservoirs with an emphasis on pore fracture geometry studies by developing fracture and microseismic estimations, Ann. Geophys., 61, 5, SE554, doi:10.4401/ag-7638.

Li, L., H. Chen and X. M. Wang (2015). Weighted-elastic-wave interferometric imaging of microseismic source location, Appl. Geophys., 12, 2, 221-234, doi:10.1007/s11770-015-0479-z.

Lienert, B. and J. Havskov (1995). A Computer Program for Locating Earthquakes Both Locally and Globally, Seismol. Res. Lett., 66, 5, 26-36, doi:10.1785/gssrl.66.5.26.

Mousavi, S. M. and G. C. Beroza (2020). A machine-learning approach for earthquake magnitude estimation, Geophys. Res. Lett., 47, 1, e2019GL085976, doi:10.1029/2019GL085976.

Mousavi, S. M. and G. C. Beroza (2022). Deep-learning seismology, Science, 377, 6607, eabm4470, doi:10.1126/science.abm4470.

Perol, T., M. Gharbi and M. Denolle (2018). Convolutional neural network for earthquake detection and location, Sci. Adv., 4, 2, e1700578, doi:10.1126/sciadv.1700578.

Schuster, C. L. (1978). Detection Within The Wellbore Of Seismic Signals Created By Hydraulic Fracturing, in SPE Annual Technical Conference and Exhibition, Society of Petroleum Engineers, Houston, SPE-7448-MS, doi:10.2118/7448-MS.

Spence, W. (1980). Relative epicenter determination using P-wave arrival-time differences, Bull. Seismol. Soc. Am., 70, 1, 171-183, doi:10.1785/BSSA0700010171.

Tian, X., Y. Chen, X. Zhang, W. Zhang et al. (2025). Focal mechanism determination by location-constrained deep learning: Application to microseismic monitoring, Geophysics, 90, 2, L31-L42, doi:10.1190/geo2024-0478.1.

van den Ende, M. P. A. and J. P. Ampuero (2020). Automated Seismic Source Characterization Using Deep Graph Neural Networks, Geophys. Res. Lett., 47, 17, e2020GL088690, doi:10.1029/2020GL088690.

Vinard, N. A., G. G. Drijkoningen and D. J. Verschuur (2021). Localizing microseismic events on field data using a U-Net-based convolutional neural network trained on synthetic data, Geophysics, 87, 2, KS33-KS43, doi:10.1190/geo2020-0868.1.

Virieux, J. and S. Operto (2009). An overview of full-waveform inversion in exploration geophysics, Geophysics, 74, 6, WCC1-WCC26, doi:10.1190/1.3238367.

Waldhauser, F. and W. L. Ellsworth (2000). A Double-Difference Earthquake Location Algorithm: Method and Application to the Northern Hayward Fault, California, Bull. Seismol. Soc. Am., 90, 6, 1353-1368, doi:10.1785/0120000006.

Wamriew, D., M. Charara and D. Pissarenko (2022). Joint event location and velocity model update in real-time for downhole microseismic monitoring: A deep learning approach, Comput. Geosci., 158, 104965, doi:10.1016/j.cageo.2021.104965.

Woo, S., J. Park, J. Y. Lee and I. S. Kweon (2018). Cbam: Convolutional block attention module, ECCV paper, Computer Vision Foundation, V. Ferrari, M. Hebert, C. Sminchisescu and Y. Belongie (Editors), Springer, Cham, 3-19, ISSN:0302-9743.

Wu, X., Y. Shi, S. Fomel, L. Liang et al. (2019). FaultNet3D: Predicting fault probabilities, strikes, and dips with a single convolutional neural network, IEEE Trans. Geosci. Remote Sens., 57, 11, 9138-9155, doi:10.1109/TGRS.2019.2925003.

Yu, S., J. Ma and W. Wang (2019). Deep learning for denoising, Geophysics, 84, 6, V333-V350, doi:10.1190/geo2018-0668.1.

Zhang, Q., W. Zhang, X. Wu, J. Zhang et al. (2022). Deep learning for efficient microseismic location using source migration-based imaging, J. Geophys. Res. Solid Earth, 127, 3, e2021JB022649, doi:10.1029/2021JB022649.

Zhang, X., J. Zhang, C. Yuan, S. Liu et al. (2020). Locating induced earthquakes with a network of seismic stations in Oklahoma via a deep learning method, Sci. Rep., 10, 1, 1941, doi:10.1038/s41598-020-58908-5.

Zhou, S. B., R. R. Chen, X. Q. Jiang and F. J. Pan (2023). 2s-GATCN: two-stream graph attentional convolutional networks for skeleton-based action recognition, Electronics, 12, 7, 1711, doi:10.3390/electronics12071711.

Zhu, W. and G. C. Beroza (2019). PhaseNet: a deep-neural-network-based seismic arrival-time picking method, Geophys. J. Int., 216, 1, 261-273, doi:10.1093/gji/ggy423.

***CORRESPONDING AUTHOR: Xiao TIAN**

East China University of Technology, Engineering Research Center for Seismic Disaster Prevention and Engineering Geological Disaster Detection of Jiangxi Province, Nanchang, China

e-mail: tianx@ecut.edu.cn